

**Materials Sciences Division, Lawrence Berkeley National Laboratory, and  
Department of Materials Science and Engineering  
University of California at Berkeley**

## **THE RESIDUAL STRESS STATE DUE TO A SPHERICAL HARD-BODY IMPACT**

***B. L. Boyce<sup>1</sup>, X. Chen<sup>2</sup>, J. W. Hutchinson<sup>2</sup>, and R. O. Ritchie<sup>1</sup>***

<sup>1</sup>Materials Sciences Division, Lawrence Berkeley National Laboratory,  
and Department of Materials Science and Engineering,  
University of California, Berkeley, CA 94720-1760, USA

<sup>2</sup>Division of Engineering and Applied Science,  
Harvard University, Cambridge, MA 02138, USA

May 2001

submitted to *Mechanics of Materials*

Work supported by the U.S. Air Force Office of Scientific Research under Grant No. F49620-96-1-0478 under the auspices of the Multidisciplinary University Research Initiative on *High Cycle Fatigue* to the University of California (for numerical modeling and fatigue analysis), the Office of Science of the U. S. Department of Energy under contract #DE-AC03-76SF00098 (for experimental diffraction results), and the Stanford Synchrotron Radiation Laboratory, operated by the Department of Energy, Office of Basic Energy Sciences (for beamtime).

# THE RESIDUAL STRESS STATE DUE TO A SPHERICAL HARD-BODY IMPACT

**B. L. Boyce<sup>1</sup>, X. Chen<sup>2</sup>, J. W. Hutchinson<sup>2</sup> and R. O. Ritchie<sup>1\*</sup>**

<sup>1</sup>Materials Sciences Division, Lawrence Berkeley National Laboratory,  
and Department of Materials Science and Engineering,  
University of California, Berkeley, CA 94720-1760

<sup>2</sup>Division of Engineering and Applied Science,  
Harvard University, Cambridge, MA 02138

## **Abstract**

The current study assesses the residual stresses and remnant damage caused by a spherical projectile impacting upon a flat surface. The immediate application of this information is to the problem of foreign object damage (FOD) associated with the ingestion of debris into an aircraft turbine engine and the subsequent reduction in component lifetime. The work is focused on two primary features: (i) the development of numerical models for the evaluation of the deformation and stresses associated with the impact process and (ii) the use of spatially-resolved residual stress measurements to verify experimentally the numerical analysis. As a first approximation, a quasi-static numerical model was developed by ignoring time-dependent effects (i.e., strain-rate sensitivity, wave and inertia effects, etc.), where the effects of velocity were approximated by adjusting the depth and diameter of the resulting impact crater to match that of actual impact craters at the corresponding velocity. The computed residual stresses and associated elastic strain gradients were compared to experimentally measured values, obtained using synchrotron x-ray diffraction methods. This comparison indicated that the quasi-static numerical analysis was adequate for moderate impact conditions (velocity = 200 m/s, energy = 2.7 J); however, under more aggressive conditions (velocity = 300 m/s, energy = 6.1 J), there was significant discrepancy between the numerical predictions and experimental measurements. Such discrepancy may be attributed to several factors that can occur at higher impact velocities, including strain-rate sensitivity, microcrack formation, and shear-band formation. A dynamic simulation, where the time-dependent effects of strain-rate sensitivity and elastic-wave interactions were approximated, provided results in closer agreement with the experimental diffraction observations.

**Keywords:** Titanium, Ti-6Al-4V, Foreign Object Damage, Impact, Residual Stress, X-ray Diffraction, Fatigue

---

\*Corresponding author. Tel: +1-510-486-5798; fax: +1-510-486-4881.  
E-mail address: [roritchie@lbl.gov](mailto:roritchie@lbl.gov) (R. O. Ritchie)

## 1. Introduction

Foreign objects ingested by turbine engines during operation can cause significant damage to compressor airfoils. Under the influence of subsequent high-cycle fatigue loading, these damage sites can lead to the premature formation and propagation of incipient cracks, which in turn can result in severe reductions in the lifetime of the component (Aydinmakine, 1994; DiMarco, 1994; Saravanamutto, 1994; Larsen et al., 1996; Cowles, 1996). Indeed, the costs associated with such foreign object damage (FOD) have been estimated at \$4 billion annually by the Boeing Corporation (Bachtel, 1998). Despite the importance of this problem, current lifetime prediction and design methodologies for turbine engines still rely principally on empirical safety factors to account for FOD, rather than using an approach based on an understanding of the salient mechanisms involved.

To develop an understanding of how FOD degrades the fatigue life of a component, several factors need to be addressed: (i) the stress concentration associated with the geometry of the damage site, (ii) the associated microstructural distortion (i.e. shear bands, local texturing), (iii) the presence and extent of incipient microcracks induced by the impact, (iv) the residual stress field and plastic damage distribution (cold work) resulting from the impact, and (v) the relaxation or redistribution of such residual stresses upon subsequent cycling.

While several investigations are currently underway to address the issues associated with stress concentration, microstructural distortion and the creation of incipient microcracks in order to characterize the influence of FOD on fatigue life (e.g., Peters et al., 2000; Ruschau, et al., 2001), the issue of the resulting stress and displacement fields created by the FOD impact has not yet been experimentally measured. It is this damage distribution which controls the initiation and early growth of fatigue cracks from FOD sites that eventually lead to the overall failure of the component. Proper characterization should provide critical mechanistic insight into the residual stress state and its influence on fatigue behavior.

The nature of the residual stresses around a surface damage site has been predominantly studied by two communities: (i) those interested in the residual stresses associated with hardness indents for measuring either resistance to cracking or prior residual stress (Salomonson et al., 1996; Suresh and Giannakopoulos, 1998; Keng, et al., 1998) and (ii) those interested in the residual stress field formed from the shot peening process (Johnson, 1968; Studman and Field, 1977; Yokouchi et al., 1983; Al-Obaid, 1990; Li et al., 1991; Kobayashi et al., 1998). The literature related to stresses around hardness indents has almost exclusively focused on the problem of the sharp indenter, which is most commonly used for estimates of cracking resistance or prior residual stress. While the analysis of the sharp indenter problem is relevant in its reliance on determining elastic-plastic response, the quasi-static velocities and non-axisymmetric geometry limit its applicability to the FOD case.

The literature on the residual stress state created by shot peening has focused on the spherical impact problem. Here, both the shape and velocity of the impact are similar

to the FOD problem, although shot peening involves multiple overlapping impacts whereas FOD is associated with a single impact. In the case of shot peening, the multiple overlapping impacts result in a stress field that is nominally equi-biaxial in the plane of the surface and varies only with depth. However, in the case of a single impact, the resulting stress field is fully three-dimensional and varies in both the depth and along the surface. It is this distinction which limits the applicability of traditional residual stress measurements techniques, such as conventional coarse-spot x-ray diffraction, layer-removal, hole-drilling, etc., to this problem, as these techniques are generally applied to less complex stress states, or stress states that vary in only one direction.

It is the purpose of the current paper to present a numerical model for the distribution of residual stresses resulting from a FOD impact and to verify such stresses using synchrotron x-ray diffraction techniques on a Ti-6Al-4V alloy subjected to sub-ballistic impacts by chrome-hardened steel spheres at velocities of 200 and 300 m/sec.

## 2. Approach

### 2.1 Material

The material studied was a Ti-6Al-4V alloy with a composition (in wt.%) of 6.30 Al, 4.17 V, 0.19 Fe, 0.19 O, 0.013 N, 0.0035 H, bal. Ti. It was received as 20-mm thick forged plates from Teledyne Titanium after solution treating 1 hr at 925°C and vacuum annealing for 2 hr at 700°C. This alloy, which has been chosen as the basis of a comprehensive military/industry/university program on *High Cycle Fatigue*, has a microstructure consisting of a bimodal distribution of ~60 vol.% primary- $\alpha$  and ~40 vol.% lamellar colonies of  $\alpha + \beta$  (Fig 1).<sup>1</sup> This microstructure displays room temperature yield and tensile strengths of 930 and 970 MPa, respectively, and a Young's modulus of 116 GPa (Eylon, 1998).

Prior to impact, 35 x 35 x 20 mm rectangular specimens were machined from the as-received plates. Machining damage was minimized by chemical milling (H<sub>2</sub>O, HNO<sub>3</sub>, and HF in a ratio of 30:10:1 at ambient temperature) to remove more than 100  $\mu$ m from each surface of the specimen, followed by a stress-relief anneal at 700°C for 2 hr (with a vacuum cool).

### 2.2 Impact Method

In this study, foreign object damage was simulated by shooting spherical projectiles onto a flat specimen surface to produce a single hemispherical damage site as shown in Figure 2. Chrome-hardened steel spheres, 3.2 mm in diameter with a Rockwell C hardness of 60, were impacted onto the flat surfaces specimens at velocities of 200 and 300 m/s (incident kinetic energies of 2.7 and 6.1 J, respectively) using a compressed-gas gun facility. These velocities represent typical in-service impact velocities on aircraft engine fan blades. The spheres were accelerated by applying gas pressures between 2 and

---

<sup>1</sup> In the context of the Air Force *High Cycle Fatigue* program, this microstructure in Ti-6Al-4V has been referred to as "solution treated and overaged" (STOA).

7 MPa. A more detailed description of the impact process, resulting damage sites, and the associated fatigue behavior can be found in Peters et al. (2000).

### 2.3 Numerical Simulation of Impact

As an initial simulation of foreign object damage, a quasi-static numerical model was established consisting of a spherical indentation on a flat surface with a static normal indentation load  $P$  (Figure 2). The indenter was modeled as rigid with a diameter equal to that of the impact experiments,  $D = 3.2$  mm. The indentation load was then removed and a crater formed with depth  $\delta$ , diameter  $w$ , and plastic pile-up height  $\delta_p$ . The size of the crater was adjusted by controlling  $P$  such that the resulting crater dimensions matched with the dimensions measured on the experimental FOD impact. The substrate material was taken to be elastic-perfectly plastic with material properties specified for the bimodal Ti-6Al-4V alloy described in the previous section. Additionally, as a first approximation, impact velocities of 200 and 300 m/s impacts were simulated by quasi-static indentations on a 35 x 35 x 20 mm rectangular specimen.

Static finite element (FEM) calculations were performed using the commercial code ABAQUS version 5.8 (Hibbit et al., 1999) based on the implicit integration method. The rigid contact surface option was used to simulate the rigid indenter, and the option for finite deformation and strain was employed. In order to simplify the model and take advantage of the axis-symmetric approach, the substrate was approximated by a cylindrical block with diameter 35 mm and depth 20 mm. An axis-symmetric mesh was developed for the specimen comprising of 4000 8-node elements. As noted above, the substrate material was taken to be elastic-perfectly plastic, with a Von Mises surface to specify yielding. Coulomb friction was invoked in all calculations, where the friction coefficient  $\mu$  is taken to be 0.1 (nearly frictionless).

At low incident velocities, as indicated in the following section, the quasi-static model yields good agreement with experimental measurements. However, for 300 m/s impact velocities where the velocity is about 1/10 of the shear wave speed of the substrate material, dynamic effects come into play. In order to account for dynamic effects such as elastic wave, inertia and strain rate effects, dynamic numerical simulations were performed by incorporating the explicit integration method into the finite element program. The rigid spherical projectile was given an initial velocity of 200 or 300 m/s, which then made contact with the substrate and bounced back in about 5  $\mu$ s with a ricocheting speed of about 22% of the incident velocity. After the impact, the residual stresses at the surface were subject to high-frequency vibrations and the steady-state residual stress field was obtained after about 1 ms. In the dynamic numerical simulation, the substrate was given the same material properties as in quasi-static finite element analysis, except that the strain rate sensitivity was included in the approach. This was analytically expressed in a power-law form as:

$$\dot{\sigma} = D \left( \frac{\sigma_y(\dot{\epsilon})}{\sigma_y^0} - 1 \right)^n \quad \text{with} \quad D = 2 \cdot 10^4 \text{ and } n = 3, \quad (1)$$

where  $\dot{\epsilon}$  is the strain rate,  $\sigma_y(\dot{\epsilon})$  is the strain-rate sensitive yield stress, and  $\sigma_y^0$  the yield stress at  $\dot{\epsilon} = 0$ , and  $D$  is a proportionality constant with units of  $s^{-1}$ . This relationship is largely consistent with the experimental data of Meyer (1984) in tension in that it shows a substantial increase in the yield stress at strain rates in excess of  $10^3 s^{-1}$ ; however, it is less linear than the experimental data of Follansbee and Gray (1989) for testing in compression.

#### 2.4 Diffraction Analysis of Residual Stress State

A primary objective in the current study was to compare the numerically predicted residual stress states to experimental observations. To this end, spatially resolved residual stress measurements were performed using synchrotron x-ray diffraction at beamline 2-1 of the Stanford Synchrotron Radiation Laboratory (SSRL). The advantage of the synchrotron source for this particular application was (a) a low divergence ( $<0.2$  mrad) source/detector configuration to minimize sample displacement errors associated with the coarse topography of the indent, and (b) a photon flux several orders of magnitude more intense than a conventional sealed-tube source, enabling sub-millimeter spatial resolution without the divergence of capillary optics.

For comparison to numerical predictions, two modes of characterization were utilized. A relatively fast measurement of the  $d$ -spacing normal to the surface yielded an estimate for the residual elastic strain component,  $\epsilon_{zz}$ , normal to the surface. In regions of particular interest, the conventional  $\sin^2\psi$  method (Prevey, 1977; Noyan and Cohen, 1987) was employed for measuring the in-plane stresses. These two techniques are described in more detail in the following paragraphs. It should be noted that all experimental comparisons to the finite element results were restricted to the specimen surface because traditional layer-removal techniques to observe the subsurface stress gradient cannot be applied here due to the three-dimensional nature of the stress gradient and crater geometry.

*Out-of-Plane Strain Measurement:* The most readily determined component of residual elastic strain is the component normal to the specimen surface,  $\epsilon_{zz}$ . Note that the  $z$ -direction is normal to the specimen surface, as shown in the coordinate axes defined in Figure 2. Under conditions of symmetric diffraction, where the incident and diffracted x-rays are at equal angles to the specimen surface, the  $d$ -spacing of planes coplanar with the specimen surface are measured. By comparing the  $d$ -spacing of a stressed region to that of an unstressed reference  $d$ -spacing, the  $\epsilon_{zz}$  component can be assessed:

$$\epsilon_{zz} = \frac{d - d_o}{d_o} = \frac{\sin \theta_o}{\sin \theta} - 1. \quad (2)$$

The measured  $\epsilon_{zz}$  values provide a comparison of the relative residual strain distributions formed under various conditions (material, velocity, indenter size, etc.). Conversion of the  $\epsilon_{zz}$  strain value to a stress requires knowledge of the stress state at that location. For example, if the stress state is equi-biaxial ( $\sigma_{rr} = \sigma_{\theta\theta}$ ), as in the case of a

shot peened surface, the stresses can be derived by using the appropriate<sup>2</sup> elastic constants:

$$\sigma_{rr} = \sigma_{\theta\theta} = \frac{E\varepsilon_{zz}}{2\nu}. \quad (3)$$

While this approach is valid when a residual stress state is known or assumed at a particular surface location (e.g. equi-biaxial at the crater floor), it is not possible to convert unambiguously the  $\varepsilon_{zz}$  values measured by this technique into stress components without some knowledge of the stress state elsewhere. Nevertheless, for the purpose of evaluating the validity of a finite element model, it may not be necessary, or beneficial, to convert to stress, but rather to directly compare the numerical and experimental values of the elastic residual strain distribution,  $\varepsilon_{zz}$ .

*Measurement of In-Plane Stresses:* In the present work, the well-documented  $\sin^2\psi$  technique (Prevey, 1977; Noyan and Cohen, 1987) was used to measure the local stresses in the plane of the specimen. In conventional powder diffraction, as well as the previously described experiment for measuring out-of-plane strain, the diffraction vector is normal to the specimen surface and the interrogated diffraction planes are coplanar with the surface, as shown in Figure 3. However, the  $\sin^2\psi$  technique interrogates crystallographic planes tilted at multiple angles,  $\psi$ , from the surface-normal. The variation in  $d$ -spacing with tilt-angle,  $\psi$  is uniquely correlated to the stress components in the interrogation volume. In the special case where  $\sigma_{zz} = \sigma_{rz} = \sigma_{\theta z} = 0$ , such as exists at a free surface, the variation in  $d$ -spacing is expected to be linear with respect to  $\sin^2\psi$ . Moreover, the slope of the linear relationship between  $d$ -spacing and  $\sin^2\psi$  is proportional to the stress component,  $\sigma_{\psi=90}$ , in the plane of the specimen, along the direction of the diffraction vector at  $\psi = 90^\circ$ :

$$\frac{d_\psi - d_0}{d_0} = \frac{1+\nu}{E} \sigma_{\psi=90} \sin^2\psi - \frac{\nu}{E} (\sigma_{rr} + \sigma_{\theta\theta}). \quad (4)$$

When this linear relationship between  $d$ -spacing and tilt angle,  $\psi$ , is observed, the corresponding stress in the plane of the specimen can be deduced. A nonlinear relationship may be an indication of non-negligible out-of-plane stresses near the free surface or strong texture and requires a more sophisticated analysis. A more complete description of the assumptions and potential errors associated with the  $\sin^2\psi$  technique is given in Noyan and Cohen (1987).

---

<sup>2</sup> For these experiments, “x-ray” elastic constants are generally generated experimentally by *in situ* loading of a tensile specimen to known levels of stress, and by correlation to the observed change in  $d$ -spacing. In the case of a crystal with anisotropic elastic constants, this calibration must be applied to the same set of planes as used for the interrogation (Prevey, 1977).

Independent validation of both the out-of-plane strain measurement technique and the  $\sin^2 \psi$  technique was achieved by applying known strain levels to a standard, similar to that used in previous diffraction-based residual stress studies (Prevey, 1977). A strain-gauged Ti-6Al-4V tensile specimen was loaded in an *in situ* tensile load frame to various levels of strain ranging from 0 to 6000  $\mu\epsilon$  corresponding to uniaxial stresses in the range of 0 to 700 MPa. The elastic strains measured by the x-ray method were found to be within 300  $\mu\epsilon$  of the observed strain gauge values. It should be noted that in the case where the diffraction vector (the bisector of the incident and diffracted beam) is normal to the specimen surface, the observed strain component is also normal to the specimen surface, and is the Poisson response to the applied strain.

### 3. Results

#### 3.1 Numerical Results

In the current study, numerical simulations were performing for two impact velocities (200 and 300 m/s), using two methods: an initial quasi-static analysis and explicit dynamic analysis. There were several general features that were consistent for both velocities and both simulation methods. The results in Figure 4 focus on the hoop stress component,  $\sigma_{\theta\theta}$ , as the hoop stress component superimposes on the applied load during fatigue crack initiation and growth (Peters et al., 2000; Chen and Hutchinson, 2001). A consistent result from the two methods was the existence at both impact velocities of two primary zones of tension in the immediate vicinity of the indent; these regions of tensile residual stress serve to increase the local mean stress during subsequent fatigue loading, thereby accelerating the initiation and propagation of fatigue cracks. These tensile zones were: (i) a small but intense region at the surface immediately outside the crater rim, and (ii) a broad region approximately one crater radius away from the crater where the maximum stresses in this region are well below the surface. In both tensile zones, the maximum tensile stress was on the order of 40% of the yield stress. The most substantial compressive stresses, conversely, are formed in a large zone directly beneath the crater, and show a maximum value of approximately 1½ times the yield stress, roughly one crater radius below the crater floor. These observations are consistent for both impact velocities.

While the quasi-static and dynamic finite element analyses predict almost identical residual stress fields away from the surface of the specimen, the results are quite different at the notch surface where the dynamic effects are of most concern. In particular, by ignoring the elastic wave and inertia effects, the quasi-static model predicted a more compressive  $\sigma_{\theta\theta}$  at the crater floor and a more tensile  $\sigma_{\theta\theta}$  at the rim, compared with dynamic simulation. Specific values of  $\sigma_{\theta\theta}$  calculated at surface locations of interest are compared with parallel experimental data in the next section. Indeed, as discussed below, the dynamic finite element simulation based on the explicit integration method is more effective in stimulating the impact process, and hence yields results closer to experimental observations. In Figures 4(a) and 4(b), contour plots of the residual hoop



stress field  $\sigma_{\theta\theta}$  around the notch, determined from dynamic finite element approach, are shown for the cases of 200 and 300 m/s impact velocities, respectively.

The prominent residual compressive stress field can also be seen in Figure 4 beneath the impact crater floor, with the stress gradient being fairly large at the surface. At the 300 m/s impact, for example, the compressive residual  $\sigma_{\theta\theta}$  stress directly below the crater was seen to vary from about  $-0.1\sigma_y^0$  at the surface of the crater floor to  $-0.8\sigma_y^0$  at  $\sim 100\ \mu\text{m}$  below the surface and continues to decrease to a maximum compressive stress of  $\sim -1.5\sigma_y^0$  at a depth of 1.4 mm, as shown in Figure 4(b). Two prominent residual tensile regions are developed after impact: one right at the crater rim, and the other located southeast of the crater rim (below the surface), where the maximum value of residual  $\sigma_{\theta\theta}$  stress is about  $0.4\sigma_y^0$ . Both regions are likely to provide fatigue crack initiation sites during subsequent cyclic loading, where the residual tensile  $\sigma_{\theta\theta}$  is proven to be one of the primary driving forces (Peters et al., 2001). The crater floor is another potential fatigue crack formation site due to the higher elastic stress concentration factor compared with the rim, especially at lower impact speeds. At high incident velocity (300 m/s), the microcracks that are formed on impact in the pile-up of material at the crater ridge, plus the residual tensile  $\sigma_{\theta\theta}$  stress field, act in concert to promote fatigue-crack growth; such growth initiates from these microcracks when the applied cyclic stresses are high compared to the magnitude of the maximum tensile residual stresses. Conversely, when the applied cyclic stresses are comparable in magnitude to the residual stress levels, fatigue cracks can initiate below the sample surface away from the impact crater, specifically in the region of high residual tensile stress (Peters et al., 2001).

### 3.2 Experimental Results

As a basis for comparison with the numerical results, the gradient in residual strain was measured from the crater rim and emanating away from the crater. To evaluate strain, the  $(21\bar{3}1)$  diffraction peak at  $\sim 110.5^\circ\ 2\theta$  (energy = 8048 keV) was chosen to provide (i) a sufficiently high  $2\theta$  angle to project a small “footprint” on the sample, (ii) a sufficient intensity to allow accurate peak fitting, and (iii) to have similar elastic behavior to that of the overall sample (unlike basal or prism planes which have significantly different elastic behavior due to crystal anisotropy). A spot size was chosen such that the projected x-ray footprint on the sample was  $500 \times 500\ \mu\text{m}$ . This spot size was a compromise between the need for small spatial scale to map out the strain gradient which varies over several millimeters, and the need for a sufficiently large spot size to sample many grains for powder diffraction analysis. During  $\psi$ -tilting experiments, the spot size was adjusted for every  $\psi$ -tilt to keep the sampling area constant. The  $500 \times 500\ \mu\text{m}$  sampling area was estimated to interrogate at least 300 grains simultaneously, whereas at least 100 grains are generally considered sufficient for powder diffraction analysis. To increase the number of grains properly oriented for diffraction, the sample was rocked  $\pm 2^\circ$  on the  $\theta$  axis for each  $2\theta$  position.

The out-of-plane strain measurement, where the diffraction vector was perpendicular to the specimen surface, was useful for mapping out the spatial distribution of the  $\epsilon_{zz}$  component normal to the surface. An example of a two-dimensional spatial strain map around a 200 m/s impact crater is shown in Figure 5. This crater map shows a local maximum tensile strain at the crater floor, which corresponds to an equi-biaxial stress of about -500 MPa (assuming that the stress state at the crater is indeed equi-biaxial and the strain normal to the surface is the Poisson response to the equi-biaxial stress).

At specific points of interest, a more thorough  $\sin^2\psi$  analysis was performed to determine the in-plane stresses,  $\sigma_{\theta\theta}$  and/or  $\sigma_{rr}$ . Because of time constraints, a spatial map of the stresses was not feasible; a two dimensional map of the in-plane stresses similar to the map presented in Figure 5 for strain would require more than three weeks of synchrotron time using the current experimental setup. An example of the variation of  $d$ -spacing with  $\sin^2\psi$  is presented in Figure 6. As is expected in the case of a negligible out-of-plane stress component and low to moderate texture, the  $d$ -spacing varies linearly with  $\sin^2\psi$ .

## 4. Discussion

### 4.1 Comparison of Numerical and Experimental Results

The primary motivation behind the experimental x-ray diffraction work was to evaluate the validity of the numerical models. For this evaluation, there were two primary modes of comparison: (i) a qualitative comparison of the spatial gradient in residual stress (or residual elastic strain) to ensure that the size-scale and nature of the stress state was captured appropriately, and (ii) a quantitative comparison of residual stress values at specific key locations to aid in understanding the driving force for crack formation and propagation.

*Qualitative comparison of gradient shape:* A comparison of the spatial gradient corresponding to three residual elastic strain components is shown in Figure 7. The relative shape of each of the three gradients is quite similar between the FEM prediction and the diffraction (XRD) analysis. A more direct comparison of the  $\epsilon_{zz}$  strain gradient emanating away from the rim is presented in Figure 8. Here, the comparison is between the diffraction data and the quasi-static FEM analysis. Again, the shape of the gradient is quite similar between experimental and numerical analysis, although at the higher impact velocity the magnitude of the predicted strains are considerably higher than the observed strains. This discrepancy, which was observed only at the higher impact velocity, is discussed in detail below.

*Quantitative comparison of stresses at key locations:* The center of the crater floor and the crater rim were two key locations for the comparison of stresses, based on evidence of crack formation in these regions during subsequent fatigue loading (Peters et al., 2000).

The role of residual stresses on fatigue crack formation at these locations was discussed in the last section. These locations were also the most challenging for both the FEM model and the x-ray diffraction experiments due to the high degree of plastic deformation. For purposes of comparison, the stress values from the numerical model were extracted from 6  $\mu\text{m}$  below the surface (the average x-ray penetration depth) and averaged over 0.5  $\text{mm}^2$  (the x-ray footprint size). The stress component of most importance is the component acting along the  $\theta$  direction,  $\sigma_{\theta\theta}$ , because it is this component which is acting in the same direction as the subsequent fatigue loading, and therefore driving fatigue-crack nucleation (Peters et al., 2000; Chen and Hutchinson, 2001).

Table 1.

Comparison of relevant stresses at key locations as predicted by the finite element method (FEM) and measured by x-ray diffraction (XRD)

<i>Method</i>	$\sigma_{rr}$ at center of crater floor (MPa)	$\sigma_{\theta\theta}$ at crater rim (MPa)	Height of crater depth + pile up (mm)
<i>200 m/s</i>			
XRD, dynamic	-523	150	0.43
FEM, quasi-static	-505	267	0.43
FEM, dynamic	-420	150	0.42
<i>300 m/s</i>			
XRD, dynamic	56	0	0.67
FEM, quasi-static	-846	503	0.67
FEM, dynamic	-82	309	0.67

The most important observation of the current study is that the quasi-static calculation of the stresses associated with a 200 m/s impact was largely consistent with experimental observation. However, there was a large discrepancy in the stress values predicted for the 300 m/s impact using the quasi-static numerical approximation. This discrepancy was reduced substantially by taking into account three time-dependent effects, specifically the strain rate sensitivity, inertia effect, and elastic wave interactions. The potential sources for the remnant discrepancy are largely non-continuum effects that are not easily captured in a continuum-based model. During the impact process and prior to fatigue loading, two features were observed in the specimens following 300 m/s impact: microcracks (2-50  $\mu\text{m}$ ) which were formed at the crater rim and shear bands that emanated into the interior of the specimen under the indent (Figure 9). These localized

effects would not be readily modeled in the continuum-based FEM calculations and would serve to reduce the intensity of the local stresses, consistent with the observed discrepancy between the FEM model and diffraction measurements. Moreover, the absence of these features for 200 m/s impacts is consistent with the agreement between the two methods at the lower velocity.

## 4.2 Implications

The residual stresses left by high velocity impacts are thought to play an important role in promoting premature fatigue failure in airfoils and fan components that have suffered foreign object damage due to the ingestion of debris into a turbine engine. Cyclic loading studies on fatigue specimens with simulated foreign object damage, identical to the hemispherical damage sites presented in this work, have shown that in many cases, knowledge of the initial residual stress distribution left by the impacting process is not sufficient to evaluate the driving force for crack formation and propagation (Peters et al., 2001). The elastic stress concentration factor,  $k_t$ , associated with the shape of the indent amplifies the applied stresses most substantially at the crater floor ( $k_t = 1.6$  from a 300 m/s impact), and at the rim ( $k_t = 1.25$  from a 300 m/s impact). Even more important is the formation of microcracks at the crater rim, which, in the simplest sense, provides a much higher (crack-like) local stress concentration factor.

Recent studies have also shown that the initial residual stress state is substantially reduced by relaxation or redistribution during subsequent fatigue cycling. For example, during fatigue loading at the smooth-bar  $10^7$ -cycle fatigue limit in the bimodal Ti-6Al-4V alloy, i.e., at  $\sigma_{\max} = 500$  MPa, the residual stresses at the rim and crater floor of an indent formed by quasi-static indentation are reduced by 30-50% after the first fatigue cycle. To probe this behavior analytically, the numerical model was modified to take into account the Bauschinger effect (non-linear cyclic stress-strain relationship with a yield surface similar to kinematic hardening) based on cyclic stress-strain experiments. The numerical model showed a very similar relaxation effect: a reduction of residual stresses on the order of 40% after the first cycle due to the change in yield surface during cycling and the consequential plastic flow leading to stress redistribution. This redistribution or first-cycle relaxation of the residual stresses is important, as it indicates that the initial residual stress state is more aggressive than the residual stress state at the time of crack initiation and propagation.

The current results also have implications to shot peening. There are many similarities (and some notable differences) between the current study, which primarily focused on the impact of a single spherical projectile on a flat surface, and the case of shot peening, where multiple spherical projectiles are impacted on a flat surface in succession. Perhaps the most noteworthy observation is the presence of significant tensile stresses at the crater rim. In the case of multiple overlapping shots, in the simplest sense, the tensile zone at the rim of a single shot is offset when the compressive crater floor of a successive shot is centered on the rim of the first. This is consistent with shot peening observations that indicate that incomplete peening coverage of the surface will leave uncompressed rims, leading to a degradation in the fatigue lifetime. As reported by

Wohlfahrt (1982), such incomplete peening coverage results in local zones of tensile residual surface stresses, which can act to promote crack formation.

## **5. Conclusions**

Based on the numerical (finite element analysis) and experimental (synchrotron x-ray diffraction) evaluation of a spherical hard-body impact on a flat surface at velocities of 200 and 300 m/s in a Ti-6Al-4V alloy, the following conclusions have been made:

1. The residual stress distribution associated with a spherical hard body impact has been modeled by quasi-static and dynamic FEM analysis. The hoop stresses, which would superimpose on applied loads along the loading axis, are tensile in two regions: (i) a small but intense region at the surface immediately outside the crater rim, and (ii) a broad region approximately one crater radius away from the crater where the maximum stresses in this region are below the surface. Substantial compressive stresses are formed in a large zone directly beneath the crater; the most intense of these are located approximately one-half a crater radius below the crater floor.
2. The maximum values of these residual stresses were found to be approximately 40% of the yield stress in both tensile regions, and  $1\frac{1}{2}$  times the yield stress in the compressive region below the base of the crater. These observations are consistent for both impact velocities.
2. The shape of the spatial strain gradient predicted by the FEM model is consistent with experimental observations made by spatially-resolved x-ray diffraction.
3. A 200 m/s impact can be modeled using a quasi-static approach, ignoring time-dependent effects and simply simulating the effect of velocity by matching the relative shape of the crater (depth-to-diameter ratio). The quasi-static model of the 200 m/s indent is quite similar to experimentally observed residual stress values and strain gradients. There is a small discrepancy ( $\sim 150$  MPa) in predicted versus measured residual stresses at the rim, which can be reduced by incorporating dynamic effects into the numerical model.
4. There are substantial errors arising from the application of a quasi-static analysis to the simulation of a 300 m/s impact. These errors are in part attributable to time-dependent effects (strain-rate sensitivity, elastic-wave interactions); indeed, they are substantially reduced by incorporating such time-dependence into the numerical model. Remnant discrepancy between the numerical model and diffraction-based results may be associated with observed non-continuum effects, such as micro-cracking and shear-band formation.

## **Acknowledgements**

This work was supported by the U.S. Air Force Office of Scientific Research under Grant No. F49620-96-1-0478 under the auspices of the Multidisciplinary University Research Initiative on *High Cycle Fatigue* to the University of California (for numerical modeling and fatigue analysis), the Office of Science, U. S. Department of Energy under contract #DE-AC03-76SF00098 (for experimental diffraction results), and the Stanford Synchrotron Radiation Laboratory, operated by the Department of Energy, Office of Basic Energy Sciences (for x-ray beamtime). Thanks are due to Dr. J. O. Peters for performing the ballistic impacts, to Dr. J. M. McNaney for assisting with the *in situ* straining experiments, and to R. K. Nalla for helpful discussions.

## References

- Al-Obaid, Y.F., 1990. A rudimentary analysis of improving fatigue life of metals by shot peening. *J. App. Mech.* 57, 307-312.
- Aydinmakine, F., 1994. Understanding and preventing failures and their causes in gas turbine engines, Technical Evaluator's Report, AGARD-CP-558, p. K.1.
- Bachtel, B., 1998. Foreign object debris and damage prevention. *Aeromagazine* 1, Article S.
- Chen, X., Hutchinson, J.W., 2001. Foreign object damage and fatigue crack threshold: cracking outside shallow indents. *Int. J. Fract.* 107, 31-51
- Cowles, B.A., 1996. High cycle fatigue in gas turbines – an industry perspective. *Int. J. Fract.* 80, 147-163.
- DiMarco, C., 1994. Navy foreign object damage and its impact on future gas turbine low pressure compression system. Technical Evaluator's Report, AGARD-CP-558, p. G.1.
- Eylon, D., 1998. Summary of the available information on the processing of the Ti-6Al-4V HCF/LCF program plates. University of Dayton Report, Dayton, OH.
- Follansbee, P.S. and Gray, G.T., 1989. An analysis of the low temperature, low and high strain-rate deformation of Ti-6Al-4V. *Metall. Trans. A*, 20A, 863-874.
- Hibbit, Karlsson & Sorensen Inc., 1999. ABAQUS version 5.8 User's Manual. Hibbit, Karlsson & Sorensen Inc., Pawtucket, RI.
- Johnson, K.L., 1968. In: Heyman, J., Leckie, F.A. (Eds.), *Engineering Plasticity*. Cambridge University Press, p. 341.
- Kobayashi, M., Matsui, T., Murakami, Y., 1998. Mechanism of creation of compressive residual stress by shot peening. *Int. J. Fatigue* 20, 351-357.

Larsen, J.M., Worth, B.D., Annis, C.G., Haake, F.K., 1996. An assessment of the role of near-threshold crack growth in high-cycle-fatigue life prediction of aerospace titanium alloys under turbine engine spectra. *Int. J. Fract.* 80, 237-255.

Li, Y.K., Mei, Y., Duo, W., Renzhi, W., 1991. Mechanical approach to the residual stress field induced by shot peening. *Mater. Sci. Eng. A147*, 167-173.

Meyer, L.W., 1984. In: Lütjering, G., Zwick, U., Bunk, W. (Eds.), *Titanium, Science and Technology*, Deutsche Gesellschaft für Metallkunde. pp. 1851-58.

Noyan, I.C., Cohen, J.B., 1987. *Residual Stress: Measurement by Diffraction and Interpretation*. Springer-Verlag, New York.

Peters, J.O., Roder, O., Boyce, B.L., Thompson, A.W., Ritchie, R.O., 2000. Role of foreign-object damage on thresholds for high-cycle fatigue in Ti-6Al-4V. *Metall. Mater. Trans. A*, 31A, 1571-1583.

Peters J.O., Ritchie, R.O., 2000. Influence of foreign-object damage on crack initiation and early crack growth during high-cycle fatigue of Ti-6Al-4V. *Eng. Fract. Mech.* 67, 193-207

Peters, J.O., Boyce, B.L., Chen, X., McNaney, J.M., Hutchinson, J.W., Ritchie, R.O., 2001. Role of residual stresses on high-cycle fatigue of impact-damaged Ti-6Al-4V: surface vs. subsurface crack initiation. In: Tschegg, S. (Ed.), *Proceedings of the International Conference on Fatigue in the Very High Cycle Regime*.

Prevey, P.S., 1977. A method of determining the elastic properties of alloys in selected crystallographic directions for x-ray diffraction residual stress measurement. *Advances in X-ray Analysis* 20, 345-354.

Ruschau, J.J., Nicholas, T., Thompson, S.R., 2001. Influence of foreign object damage (FOD) on the fatigue life of simulated Ti-6Al-4V airfoils. *Eng. Fract. Mech.* 25, 233-250.

Salomonson, J., Zeng, K., Rowcliffe, D., 1996. Decay of residual stress at indentation cracks during slow crack growth in soda-lime glass. *Acta Mater.* 44, 543-546.

Saravanamutto, H.I.H., 1994. Erosion, corrosion and foreign object damage in gas turbines. Technical Evaluator's Report, AGARD-CP-558, p. T.1.

Studman, C.J., Field, J.E., 1977. The indentation of hard metals: the role of residual stresses. *J. Mater. Sci.* 12, 215-218.

Suresh, S., Giannakopoulos, A.E., 1998. A new method for estimating residual stress by instrumented sharp indentation. *Acta Mater.* 46, 5755-5767.

Wohlfahrt, H., 1982. Shot peening and residual stress. In: Kula, E., Weiss, V. (Eds.), *Residual Stress and Stress Relaxation*, Sagamore Army Materials Research Conference Proceedings, Plenum Press, New York, pp. 1-18.

Yokouchi, Y., Chou, T.W., Greenfield, I.G., 1983. Elastic-plastic analysis of indentation damages in copper: work hardening and residual stress. *Metall. Trans. A*, 14A, 2415-2421.

Zeng, K., Giannakopoulos, A.E., Rowcliffe, D., Meier, P., 1998. Residual stress fields at the surface of sharp pyramid indentations. *J. Am. Ceramic Soc.* 81, 689-694.



## LIST OF FIGURE CAPTIONS

**Fig. 1.** Two-phase microstructure of the bimodal Ti-6Al-4V alloy under investigation consisting of HCP  $\alpha$  (light gray) and BCC  $\beta$  (dark gray). The  $\alpha$ -phase exists in both the globular primary- $\alpha$  phase and the lamellar colonies of alternating  $\alpha$  and  $\beta$ .

**Fig. 2.** Illustration of impact of a spherical indenter of diameter,  $D$ , with incident velocity  $V$  (or in the case of quasi-static loading, under normal load,  $P$ ), on a flat surface resulting in a crater of width,  $W$ , depth below the nominal surface,  $\delta$ , and pile-up above the nominal surface,  $\delta_p$ . While the residual stress field throughout the body is of interest, only the near-surface layers can be probed with x-ray diffraction. Traditional layer-removal techniques cannot be applied due to the three-dimensional nature of the stress gradient and geometry.

**Fig. 3.** Illustration of (a) general powder diffraction where the incident and exiting beams make equal angles with the specimen surface and the diffraction vector ( $\mathbf{k}-\mathbf{k}_0$ , dotted line) is perpendicular to the surface. In this case, the interrogated planes are coplanar with the specimen surface and the observed strain component is normal to the specimen surface along the direction of the diffraction vector. (b) By tilting to non-zero  $\psi$  angles, the planes of interrogation are no longer coplanar with the surface, and again the  $d$ -spacings are measured in the direction of the diffraction vector.

**Fig. 4.** Contour plots of the residual  $\sigma_{\theta\theta}$  stress field in the vicinity of crater floor predicted from dynamic finite element analysis, showing the stress distribution for (a) 200 m/s and (b) 300 m/s impact velocities. The residual stress fields are normalized by the yield stress at zero strain rate,  $\sigma_y^0$ .

**Fig. 5.** Two views of a two-dimensional surface-normal strain ( $\epsilon_{zz}$ ) survey around a site of damage formed from a 200 m/s impact. The tensile value of  $\epsilon_{zz}$  at the center of the impact crater is the Poisson strain response to the equi-biaxial compressive stresses that exist at the center of the crater floor.

**Fig. 6.** Variation of  $d$ -spacing with tilt-angle,  $\psi$ , as sampled next to the crater rim. This linear behavior is typically observed for both 200 m/s and 300 m/s impact velocities.

**Fig. 7.** Spatial gradient in elastic strain components,  $\epsilon_{rr}$ ,  $\epsilon_{\theta\theta}$ , and  $\epsilon_{zz}$ , emanating away from the crater rim as predicted by the finite element method, FEM (line), and observed by x-ray diffraction, XRD (points). In the diffraction results,  $\epsilon_{zz}$  was obtained by symmetric diffraction,  $\epsilon_{rr}$  was obtained from the  $\sin^2\psi$  technique, and  $\epsilon_{\theta\theta}$  was calculated from the other two data sets, assuming that  $\sigma_{zz} = 0$  in the interrogation volume ( $<10 \mu\text{m}$  from the free surface). For all three components of strain, the shape of the gradient, as well as the relative location of extremes, are consistent between numerical predictions and experimental observations.

**Fig 8.** Comparison of  $\epsilon_{zz}$  strain gradients observed by x-ray diffraction (data points) and predicted by FEM (lines) using a quasi-static analysis. While the gradient associated with the 200 m/s impacts appears to be in agreement between the two methods, the magnitude of the 300 m/s impact gradient is not well captured by the quasi-static analysis.

**Fig 9.** Features found in 300 m/s impacts but not in 200 m/s impacts which are not captured in the FEM model. (a) SEM micrograph of a  $\sim 6 \mu\text{m}$  microcrack formed at the crater rim due to the impact process (insert) and the subsequent growth of the microcrack to  $50 \mu\text{m}$  during fatigue loading (nominally applied  $\sigma_{\text{max}} = 500 \text{ MPa}$ ,  $R = 0.1$ ,  $N = 29,000$  cycles). (b) Optical cross-section of the crater floor showing shear band formation along planes of maximum shear (courtesy J. O. Peters).

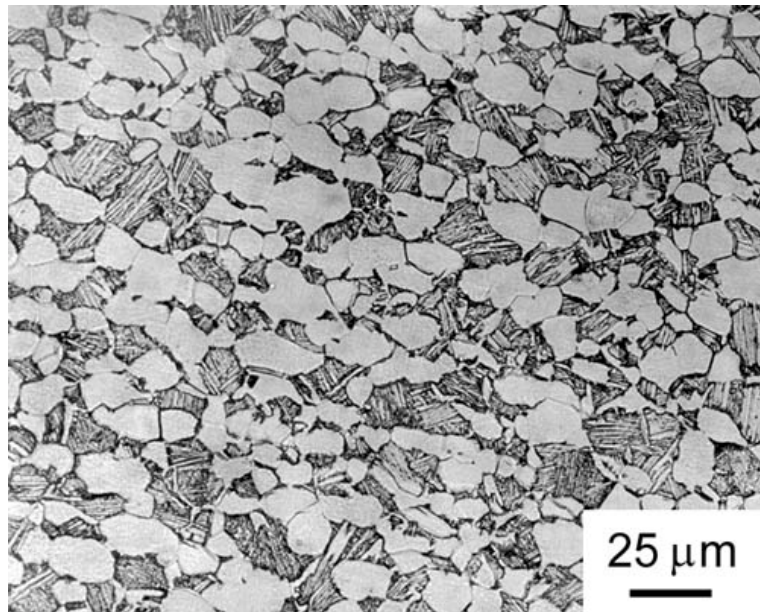


**Fig. 1.** Two-phase microstructure of the bimodal Ti-6Al-4V alloy under investigation consisting of HCP  $\alpha$  (light gray) and BCC  $\beta$  (dark gray). The  $\alpha$  exists in both the globular primary- $\alpha$  phase and the lamellar colonies of alternating  $\alpha$  and  $\beta$ .

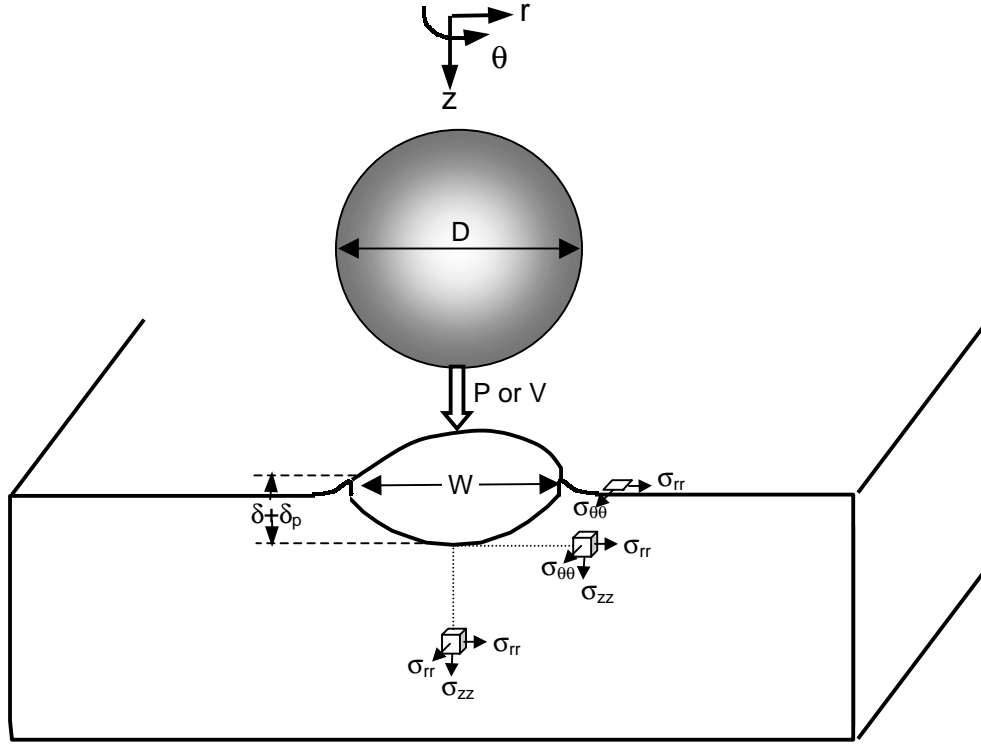


**Fig. 2.** Illustration of impact of a spherical indenter of diameter,  $D$ , with incident velocity  $V$  (or in the case of quasi-static loading, under normal load,  $P$ ), on a flat surface resulting in a crater of width,  $W$ , depth below the nominal surface,  $\delta$ , and pile-up above the nominal surface,  $\delta_p$ . While the residual stress field throughout the body is of interest, only the near-surface layers can be probed with x-ray diffraction. Traditional layer-removal techniques cannot be applied due to the three-dimensional nature of the stress gradient and geometry.

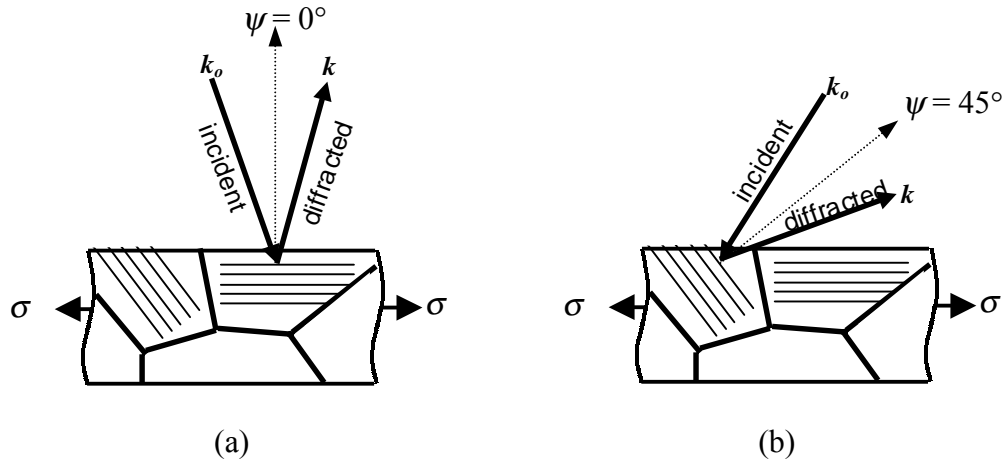
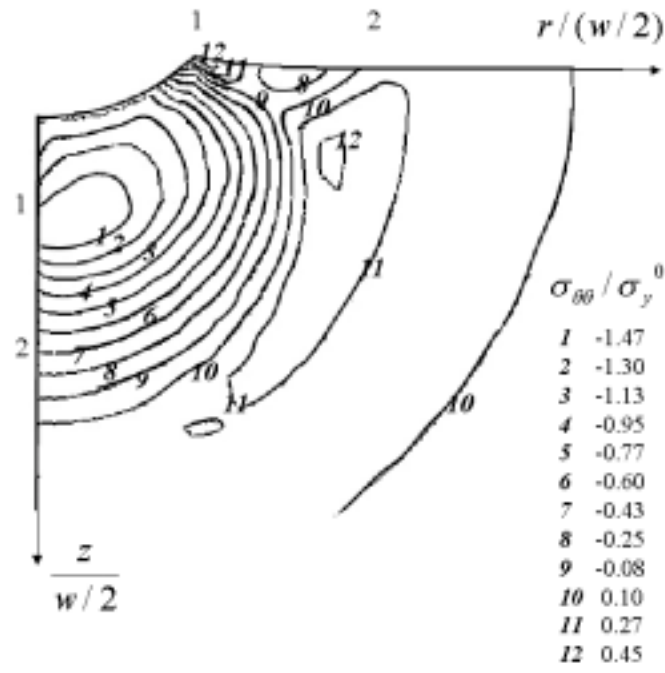
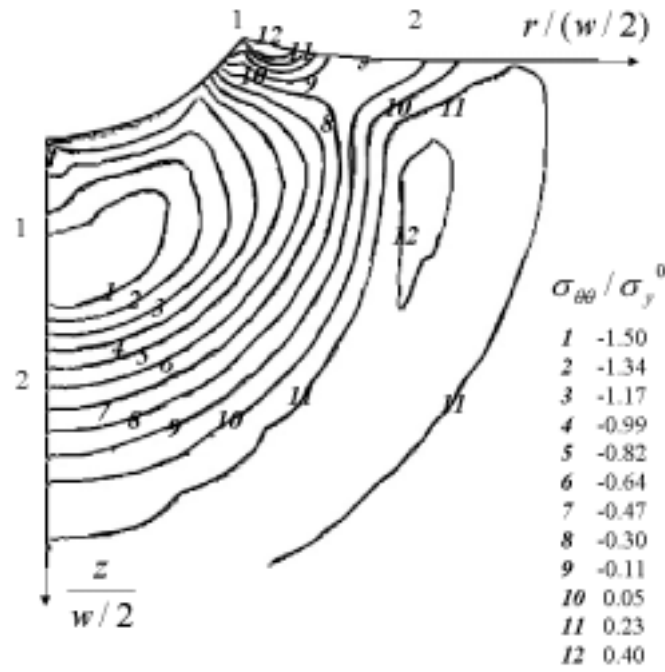


**Fig. 3.** Illustration of (a) general powder diffraction where the incident and exiting beams make equal angles with the specimen surface and the diffraction vector ( $\mathbf{k}-\mathbf{k}_o$ , dotted line) is perpendicular to the surface. In this case, the interrogated planes are coplanar with the specimen surface and the observed strain component is normal to the specimen surface along the direction of the diffraction vector. (b) By tilting to non-zero  $\psi$  angles, the planes of interrogation are no longer coplanar with the surface, and again the  $d$ -spacings are measured in the direction of the diffraction vector.



(a)



(b)

**Fig. 4.** Contour plots of the residual  $\sigma_{\theta\theta}$  stress field in the vicinity of crater floor predicted from dynamic finite element analysis, showing the stress distribution for (a) 200 m/s and (b) 300 m/s impact velocities. The residual stress fields are normalized by the yield stress at zero strain rate,  $\sigma_y^0$ .

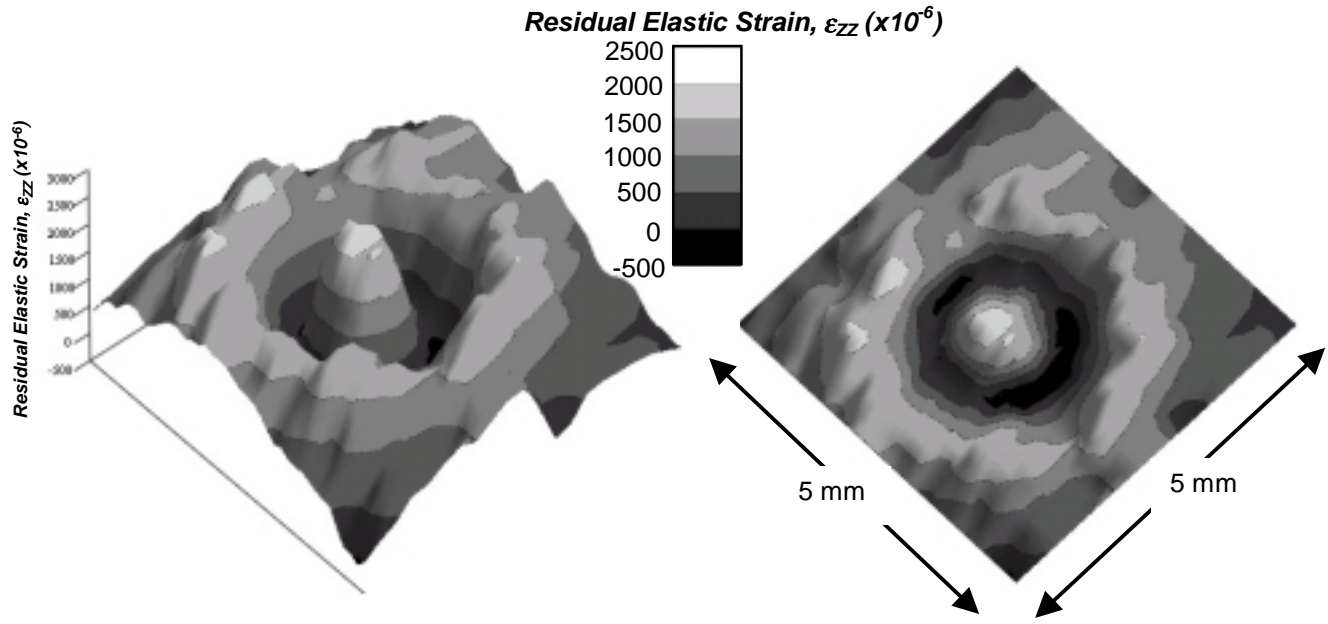


**Fig. 5.** Two views of a two-dimensional surface-normal strain ( $\epsilon_{zz}$ ) survey around a site of damage formed from a 200 m/s impact. The tensile value of  $\epsilon_{zz}$  at the center of the impact crater is the Poisson strain response to the equi-biaxial compressive stresses that exist at the center of the crater floor.

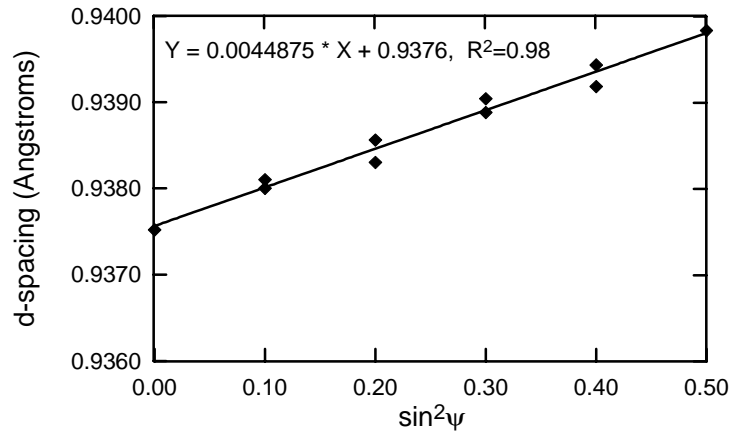


**Fig. 6.** Variation of d-spacing with tilt-angle,  $\psi$ , as sampled next to the crater rim. This linear behavior is typically observed for both 200 m/s and 300 m/s impact velocities.

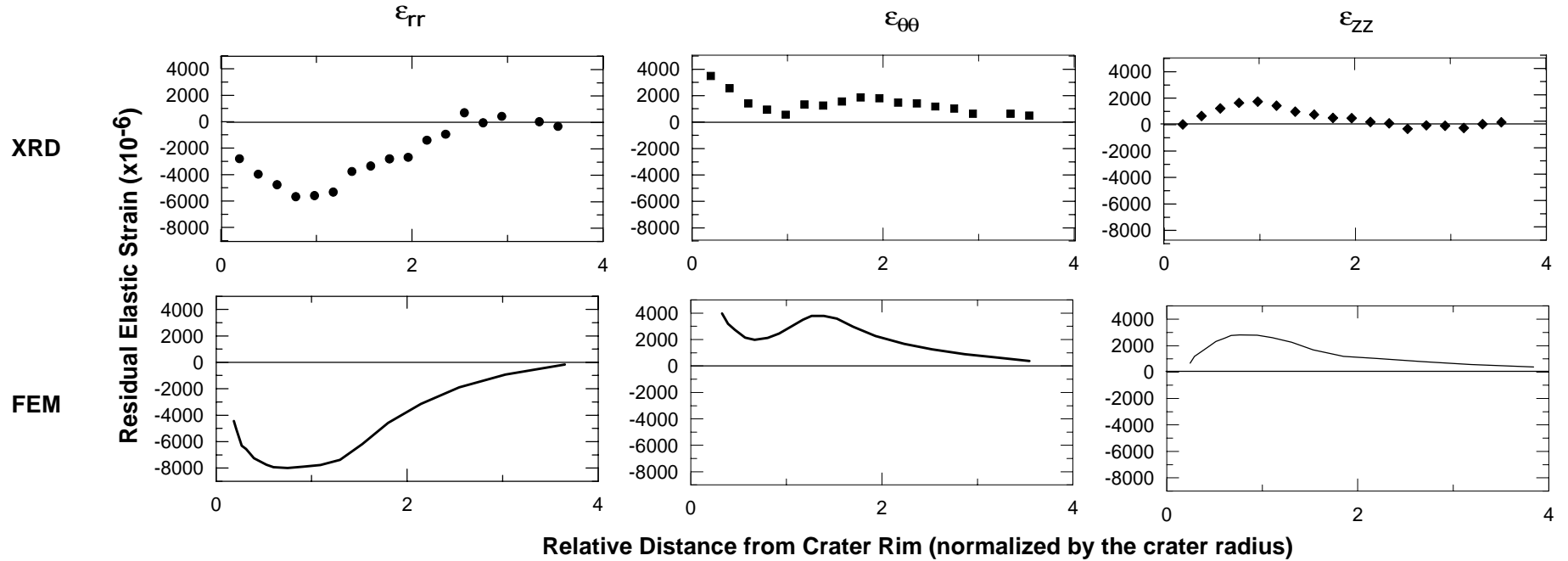


**Fig. 7.** Spatial gradient in elastic strain components,  $\epsilon_{rr}$ ,  $\epsilon_{\theta\theta}$ , and  $\epsilon_{zz}$ , emanating away from the crater rim as predicted by the finite element method, FEM (line), and observed by x-ray diffraction, XRD (points). In the diffraction results,  $\epsilon_{zz}$  was obtained by symmetric diffraction,  $\epsilon_{rr}$  was obtained from the  $\sin^2\psi$  technique, and  $\epsilon_{\theta\theta}$  was calculated from the other two data sets, assuming that  $\sigma_{zz} = 0$  in the interrogation volume ( $<10\ \mu\text{m}$  from the free surface). For all three components of strain, the shape of the gradient as well as the relative location of extremes are consistent between numerical predictions and experimental observations.



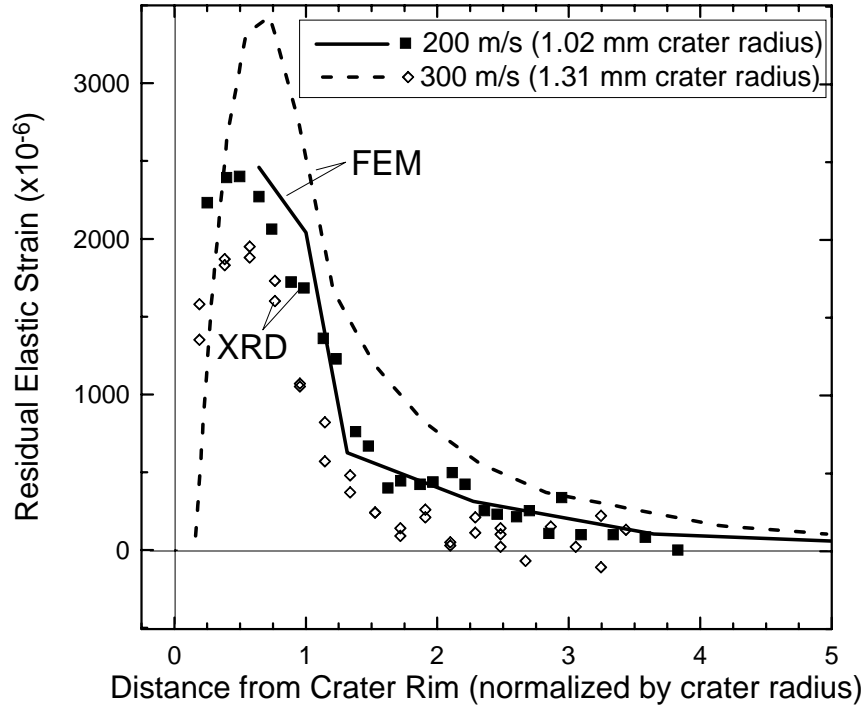


**Fig 8.** Comparison of  $\epsilon_{zz}$  strain gradients observed by x-ray diffraction (data points) and predicted by FEM (lines) using a quasi-static analysis. While the gradient associated with the 200 m/s impacts appears to be in agreement between the two methods, the magnitude of the 300 m/s impact gradient is not well captured by the quasi-static analysis.

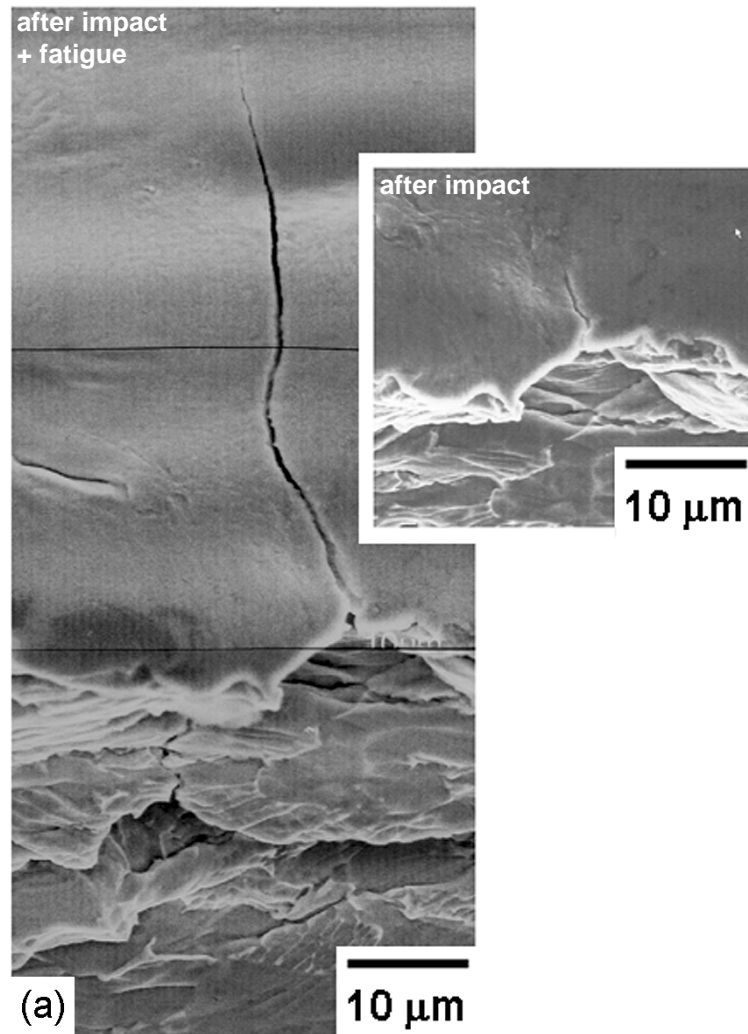


**Fig 9.** Features found in 300 m/s impacts but not in 200 m/s impacts which are not captured in the FEM model. (a) SEM micrograph of a  $\sim 6 \mu\text{m}$  microcrack formed at the crater rim due to the impact process (insert) and the subsequent growth of the microcrack to  $50 \mu\text{m}$  during fatigue loading (nominally applied  $\sigma_{\text{max}} = 500 \text{ MPa}$ ,  $R = 0.1$ ,  $N = 29,000$  cycles).

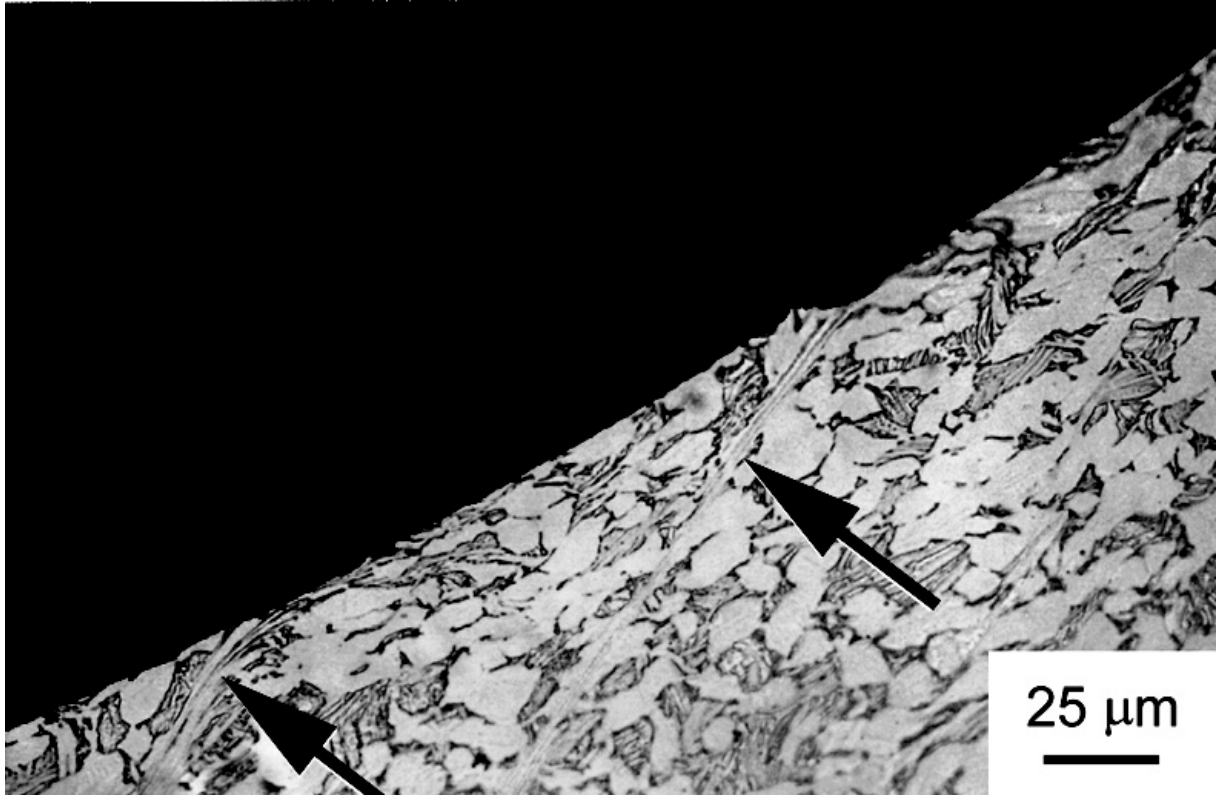


**Fig 9.** (b) *Optical cross-section of the crater floor showing shear band formation along planes of maximum shear (courtesy J. O. Peters).*